*Journal of Earth Science*, *Vol. 36*, *No. 2*, *p. 812–822*, *April 2025* *ISSN 1674-487X*
*Printed in China*
https://doi.org/10.1007/s12583-024-0146-5

# Editorial

# 3D Coseismic Deformation and Fault Slip Model of the 2023 Kahramanmaraş Earthquake Sequence Constrained by GPS, ALOS-2 and Sentinel-1 Data

**Chengyuan Bai, Wenbin Xu*, Lei Zhao, Kai Sun, Lei Xie**
*School of Geosciences and Info-Physics*, *Central South University*, *Changsha* 410083, *China*
Chengyuan Bai: https://orcid.org/0009-0005-1068-3874; Wenbin Xu: https://orcid.org/0000-0001-7294-8229

## 0 INTRODUCTION

Turkey is located at the intersection of the Eurasian, Anatolian, Arabian, and African tectonic plates. Due to the ongoing northward compression from the Arabian Plate, the Anatolian Plate is pushed westward in a tectonic escape mechanism, leading to the formation of the North Anatolian fault zone (NAFZ) and the East Anatolian fault zone (EAFZ) (e.g., Bayrak et al., 2015; Duman and Emre, 2013; Reilinger et al., 2006). The EAFZ is a nearly vertical, left-lateral strike-slip fault zone that runs about 600 km in a northeast-southwest orientation across eastern Turkey, accommodating the relative movement between the Anatolian and Arabian plates. The slip rate along the EAFZ decreases from ~10 mm/yr in the northeast to ~4.5 mm/yr in the south (Aktug et al., 2016). In contrast to the NAFZ, which has experienced significant seismic activity, including the significant earthquakes of 1939 $M_W$7.8 in Erzincan, 1999 $M_W$7.9 in Izmit and *M*w 7.2 in Düzce, the EAFZ has been relatively inactive over the last century, with the last major event occurring in 1893 (*M*7.1). This lack of seismicity suggests that substantial stress has built up along the EAFZ (Simão et al., 2016; Duman and Emre, 2013). Nalbant et al. (2002) calculated the stress changes along the EAFZ due to seismic and tectonic forces since 1822 and identified two segments with high-stress levels. The first segment, located between Elazig and Bingol, was involved in the 2020 $M_W$6.8 earthquake (Bletery et al., 2020). The second segment, found between Kahramanmaraş and Malatya, is considered to have the potential to generate an earthquake of $M_W$7.3 or greater (Aktug et al., 2016; Nalbant et al., 2002).

On February 6, 2023, the Kahramanmaraş region in south-central Turkey was hit by two significant earthquakes (Chen et al., 2023; Kusky et al., 2023). The initial quake, registering a magnitude of $M_W$7.8, occurred at 4 : 17 am local time along the southern section of the EAFZ. Nearly nine hours later, a second earthquake, with a magnitude of $M_W$7.7, shook the Savrun-Çardak fault, located approximately 90 km northeast of the epicenter of the first quake. These two seismic events, along with their subsequent aftershocks, led to the loss of at least 50 000 lives, making it the most powerful seismic event in Turkey in over 80 years. Following the Kahramanmaraş earthquake sequence, numerous researchers have employed Interferometric Synthetic Aperture Radar (InSAR) and Global Positioning System (GPS) to study the coseismic ground deformation and invert for fault slip distribution (e.g., Barbot et al., 2023; He et al., 2023; Jia et al., 2023). The findings indicate that the Amanos, Pazarcık, and Erkenek faults, which ruptured during the *M*w 7.8 event, are nearly vertical, while the Savrun, Çardak, and Söğüt faults associated with the $M_W$7.7 event exhibit a north-dipping configuration. Both events were dominated by left-lateral strike-slip motion, with most of the coseismic slip occurring at depths shallower than 20 km and the maximum slip primarily concentrated at 4–8 km.

Coseismic slip models that utilize near-field geodetic data have shown that the Pazarcık, Savrun, and Çardak faults exhibit a shallow slip deficit (SSD), which refers to a decrease or absence of coseismic slip in the shallow crust during seismic events (e.g., Jiang et al., 2024; Barbot et al., 2023; Jia et al., 2023). The SSD estimates for the Kahramanmaraş earthquake sequence vary widely among different studies, with values reported from negligible amounts up to 50%. Previous studies have demonstrated that near-field observations are essential for precise SSD estimations (Xu et al., 2016). However, disparities in SSD estimates persist, even after accounting for near-field deformation constraints (Ma et al., 2024; Jia et al., 2023). In addition, Wang et al. (2024) highlighted that the biases in near-fault data in pixel offset tracking (POT) can also affect SSD estimation, with the use of unbiased near-fault data resulting in significantly lower SSD values. Accurate estimation of SSD is crucial for understanding the seismogenic structure and assessing seismic hazards.

Here, we first applied the Differential Interferometric Synthetic Aperture Radar (DInSAR) technique to obtain the coseismic deformation field from both the ascending

*Corresponding author: wenbin.xu@csu.edu.cn


Manuscript received November 26, 2024.
Manuscript accepted December 23, 2024.

Bai Chengyuan, Xu Wenbin, Zhao Lei, Sun Kai, Xie Lei, 2025. 3D Coseismic Deformation and Fault Slip Model of the 2023 Kahramanmaraş Earthquake Sequence Constrained by GPS, ALOS-2 and Sentinel-1 Data. *Journal of Earth Science*, 36(2): 812–822. https://doi.org/10.1007/s12583-024-0146-5. http://en.earth-science.net

and descending tracks of the ALOS-2 data. Subsequently, POT was used to capture the range and azimuth offsets from both ALOS-2 and Sentinel-1 images. Using the coseismic deformation data obtained from InSAR and POT, we reconstructed the 3D deformation field of the Kahramanmaraş earthquake sequence using a weighted least squares method. Then, we integrated GPS, InSAR, and POT data to determine and invert the fault geometry and slip distribution of the 2023 Kahramanmaraş earthquake sequence and discuss the reasons behind the notable difference in SSD estimates (Figure 1).

## 1 DATA AND METHODS

### 1.1 Geodetic Data and Processing

The GPS data were collected from the Nevada Geodetic Laboratory (Blewitt et al., 2018). The SAR data utilized in this study include L-band ALOS-2 data acquired in ScanSAR mode from the Japan Aerospace Exploration Agency (JAXA) and C-band Sentinel-1 data in TOPS mode from the European Space Agency (ESA) (see Table S1). All SAR data were processed using the GAMMA software (Xu et al., 2018; Werner et al., 2000).

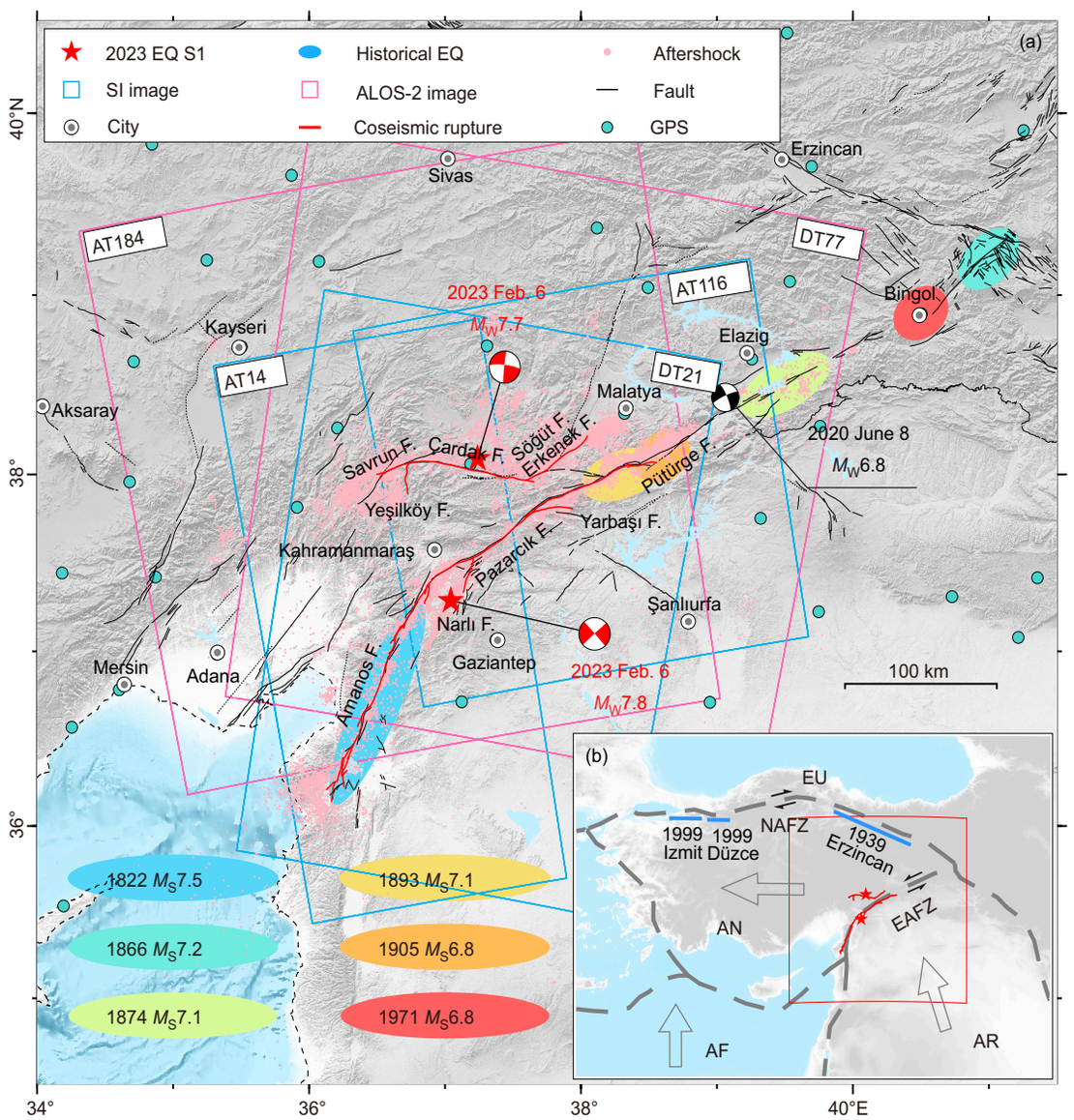


**Figure 1.** (a) Regional tectonic map of the Kahramanmaraş earthquake sequence. The red stars and red beach balls represent the epicenter and the focal mechanism of the Kahramanmaraş earthquake sequence, respectively (https://deprem.afad.gov.tr/event-focal-mechanism). The black beach ball represents the focal mechanism of the $M_W$6.8 earthquake on June 8, 2020, and the pink dots denote the relocated aftershocks from February 6, 2023, to May 31, 2023 (Lomax, 2023). The ellipses represent the rupture areas that occurred along the EAFZ between 1822 and 2001. The blue and purple boxes represent the data coverage of Sentinel-1 and ALOS-2, respectively. The red solid line illustrates the surface rupture trace of the coseismic fault (Reitman et al., 2023), the black solid lines indicate active faults, and the cyan dots are the GPS stations used in this study. Inset, the location of the Kahramanmaraş earthquake sequence. Red box corresponds to the area shown in (a). EU represents the Eurasian Plate; AN represents the Anatolian Plate; AF represents the African Plate; AR represents the Arabian Plate; blue lines denote the approximate rupture extent of historical events.

The significant deformation caused by the Kahramanmaraş earthquake sequence resulted in severe decorrelation in the Sentinel-1 data in the near-field of the fault (Jiang et al., 2024), so we did not use the phase information from Sentinel-1 data. In contrast, the ALOS-2 data, with a longer wavelength of ~23 cm compared to Sentinel-1's 5.5 cm, retains higher coherence and is better suited for capturing the associated ground displacement. We first processed the ALOS-2 data using the DInSAR technique to obtain the line-of-sight (LOS) coseismic deformation field for the Kahramanmaraş earthquake sequence. During the differential interferometry, the interferograms were multilooked with 4 looks in the range direction and 20 looks in the azimuth direction to improve the signal-to-noise ratio (SNR). The Shuttle Radar Topography Mission (SRTM) Digital Elevation Model (DEM) with one-arc second resolution was used to simulate and remove the topographic phase. After applying the Goldstein filter method to the interferograms, we used the minimum cost flow method to unwrap the phase by masking the areas with discontinuous interference fringes and coherence values below 0.1 (Chen and Zebker, 2002; Goldstein and Werner, 1998). Long-wavelength atmospheric and orbital errors were corrected by fitting polynomials in the stable far-field region.

While the long-wavelength ALOS-2 data was able to capture most of the coseismic deformation from the Kahramanmaraş earthquake sequence, it failed to recover the coseismic deformation in some near fault areas. To address this, we applied the POT method to process the amplitude images from all SAR data to measure surface displacement in the vicinity of the seismic rupture. This method is crucial for understanding the fault geometry and refining the shallow slip distribution of the fault (e.g., He et al., 2022; Merryman Boncori, 2019; Xu et al., 2018). For the ALOS-2 data, the search window was set to 64 pixels in the range direction and 320 pixels in the azimuth direction, with sampling intervals of 4 pixels for range and 20 pixels for azimuth. In Sentinel-1 data, the search window was set to 240 pixels in the range direction and 60 pixels in the azimuth direction, with sampling intervals of 20 pixels for range and 5 pixels for azimuth. To further reduce noise, we excluded pixels with offsets exceeding 5 m and applied median filtering with window sizes of 50 × 50 for ALOS-2 and 30 × 30 for Sentinel-1.

Combining the ALOS-2 ascending and descending coseismic deformation fields and the offset results from all SAR images, we reconstructed a 3D deformation field covering both the $M_W$7.8 and $M_W$7.7 events using the weighted least squares method (Hu et al., 2014). The weights for each observation used to construct the 3D deformation are determined based on the variance within a 9 × 9 window, with the window size of 9 × 9 chosen to balance computational efficiency and accuracy. The observations obtained from SAR data can be expressed as

$$\begin{bmatrix} d_{LOS} \\ d_{azi} \end{bmatrix} = \begin{bmatrix} \cos\theta & \sin\theta\sin\alpha & -\sin\theta\cos\alpha \\ 0 & \cos\alpha & \sin\alpha \end{bmatrix} \begin{bmatrix} UD \\ NS \\ EW \end{bmatrix} \quad (1)$$

where $d_{LOS}$ and $d_{azi}$ represent the observed LOS and azimuthal displacements, respectively, while *UD*, *EW*, and *NS* are the projected surface displacement components in the vertical, east-west, and north-south directions, respectively. $\theta$ and $\alpha$ denote the incidence angle and the flight azimuth angle of the SAR sensor, respectively.

### 1.2 Inversion Strategy

In an elastic half-space, the source parameters of the finite fault model include geometric parameters such as fault length, width, depth, dip angle, strike angle, and the location of the epicenter, as well as kinematic parameters such as rake angle and slip amplitude (Li et al., 2022; Okada, 1985). The two-step inversion procedure is widely used in source modelling, which includes a nonlinear inversion based on a uniform slip model followed by a linear inversion using a distributed slip model (e. g., Fang et al., 2024; He et al., 2024; Xu et al., 2022). First, a nonlinear inversion was performed to determine the geometric parameters and uniform slip of the seismogenic fault. Given that both the $M_W$7.8 and $M_W$7.7 events reached the surface (Reitman et al., 2023), the location, length, and strike angle are fixed according to the surface rupture traces. Then, the fault plane was discretized into small patches, and a linear inversion was applied to obtain the slip distribution on these patches. Finally, the coseismic fault slip distribution was linearly inverted using the Steepest Descent Method (Wang et al., 2013).

To improve inversion efficiency, the InSAR observations were downsampled using a quadtree subsampling method based on significance (Gao et al., 2021; Jónsson, 2002). For ease of analysis, the dip angles for the Amanos, Pazarcık, Erkenek, and Narlı faults were set at 90°, while the Yeşilköy fault was assigned a dip angle of 70° following previous studies (Jia et al., 2023). The dip angles for the Yarbaşı, Söğüt, Çardak, and Savrun faults were determined through a grid search. Using the minimum residual principle, the final dip angle for the Yarbaşı fault was found to be 61° southward, and for the Söğüt, Çardak, and Savrun faults, it was 59° northward. The fault planes were modeled to a depth of 20 km and discretized into 4 km × 4 km patches. The optimal smoothing factor (Figure S1a) was determined through a trade-off analysis between model roughness and misfit (Jónsson et al., 2002). The weight ratio of GPS data to InSAR data (Figure S1b) was set at 10 : 1 (Wang and Fialko, 2014). The rake angle for the Yeşilköy fault was constrained to [-90°, 90°], while the rake angles for other faults were constrained to [-45°, 45°].

## 2 RESULTS

### 2.1 3D Coseismic Deformation

The coseismic deformation fields from the ALOS-2 ascending and descending tracks (Figures S2a, S2b) show that the deformation patterns on either side of the fault are opposite, indicating that both the $M_W$7.8 and $M_W$7.7 events predominantly involved strike-slip movement. Despite the $M_W$7.7 event being of lower magnitude

than the $M_W$7.8 event, it resulted in greater surface displacements. The most significant deformation along both tracks, located north of the $M_W$7.7 event, measured 3.3 m (toward the satellite) and -3.7 m (away from the satellite), respectively. The deformation on the northern side of the Söğüt, Çardak, and Savrun faults associated with the $M_W$7.7 event is significantly larger than that on the southern side. In contrast, the LOS deformation on both sides of the faults associated with the $M_W$7.8 event is more symmetrical in magnitude and distribution. To assess the accuracy of the InSAR observations, we projected the coseismic deformations measured by GPS onto the LOS direction and compared them with the InSAR data (Figure S2c). The calculated root mean square (RMS) values for the ALOS-2 ascending and descending tracks were 7.1 and 6.8 cm, respectively.

The azimuth offsets from POT successfully address the limitations of InSAR in monitoring north-south deformation (Figure S3). The POT results clearly show the distribution of surface rupture traces, with the $M_W$7.8 event resulting in approximately 300 km of surface rupture and the $M_W$7.7 event causing approximately 150 km of surface rupture. Compared with GPS data, the RMS values of the range offsets for ALOS-2 ascending and descending tracks, and Sentinel-1 tracks 14, 116, and 21 are 12.7, 19.2, 13.9, 17.5, and 12.6 cm, respectively. The RMS values of the azimuth offsets for ALOS-2 ascending and descending tracks, and Sentinel-1 tracks 14 and 21 are 25.6, 25.4, 20.1, and 22.7 cm, respectively. The 3D deformation fields (Figures 2a–2c) show that the coseismic surface deformation caused by the Kahramanmaraş earthquake sequence is primarily horizontal. The $M_W$7.7 event was primarily characterized by east-west deformation, with the maximum westward deformation on the

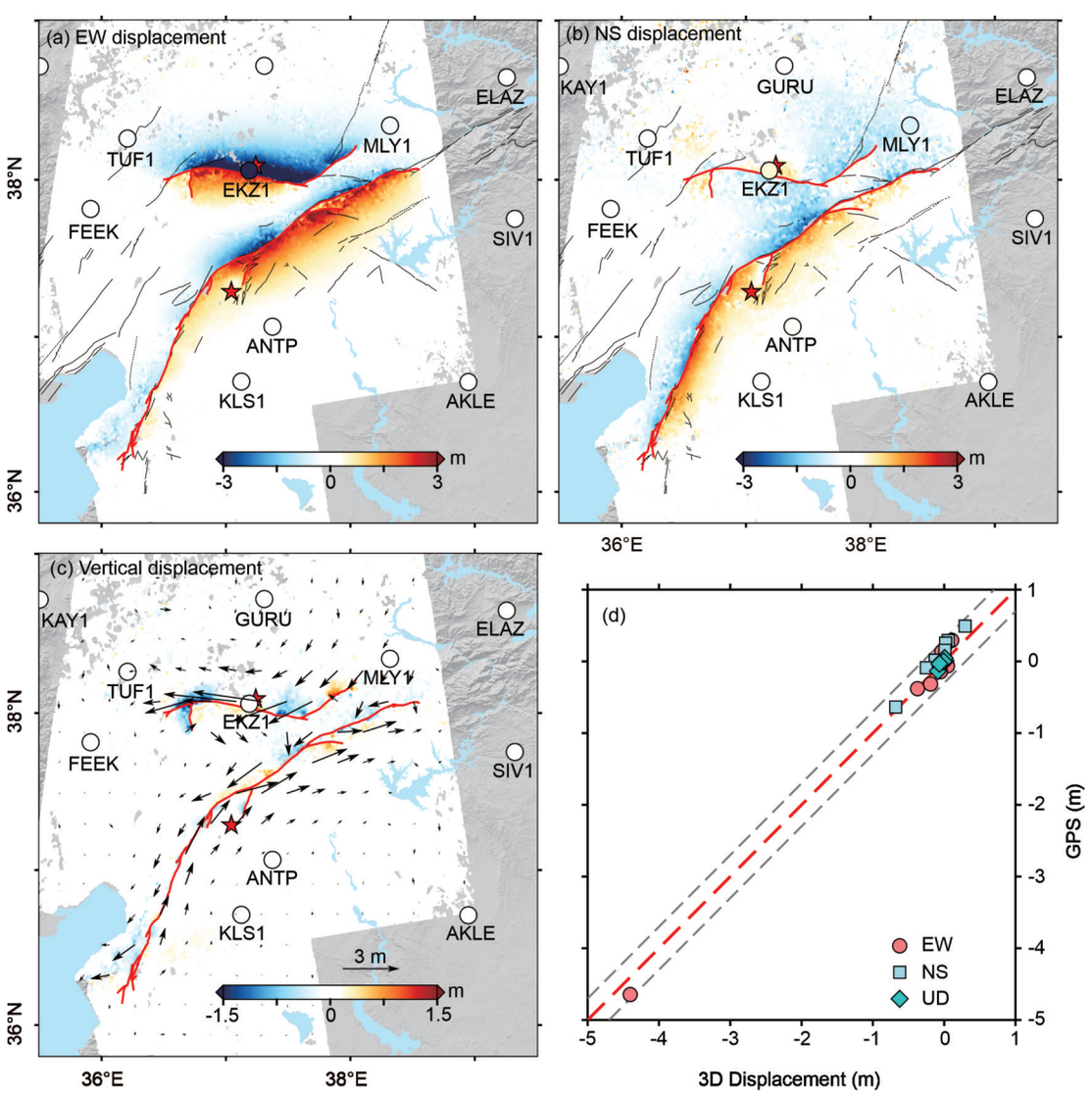


**Figure 2.** 3D coseismic ground displacement map of the 2023 Kahramanmaraş earthquake sequence, (a)–(c) illustrate the East-West, North-South, and vertical displacements, respectively. The colored circles in (a)–(c) represent the corresponding GPS 3D displacements. The arrows in (c) represent the horizontal displacements calculated from (a) and (b). (d) presents a comparison between GPS 3D displacements and SAR-derived 3D displacements.

northern side of the fault reaching 5 m, while the southern side experienced a maximum eastward deformation of 2.5 m. The Pazarcık and Erkenek faults related to the $M_W$7.8 event also show primarily east-west deformation, along with some north-south deformation, while the Amanos fault primarily exhibits north-south deformation. The vertical deformation from the $M_W$7.7 event is more pronounced and is mainly concentrated at the bends of nearby faults, with approximately 1.5 m of subsidence observed on the northern side of the Savrun fault and around 1 m on the western side of the Yeşilköy fault. We compared the 3D deformation calculated from InSAR and POT with GPS data (Figure 2d) and found the RMS values for the east-west, north-south, and vertical directions to be 15, 17, and 3 cm, respectively.

## 2.2 Coseismic Slip Model

The coseismic fault slip model (Figure 3) indicates that the overall Kahramanmaraş earthquake sequence is characterized by left-lateral strike-slip motion. For the $M_W$7.8 event, two major asperities were identified along the Pazarcık and Erkenek faults, with peak slips of 8.5

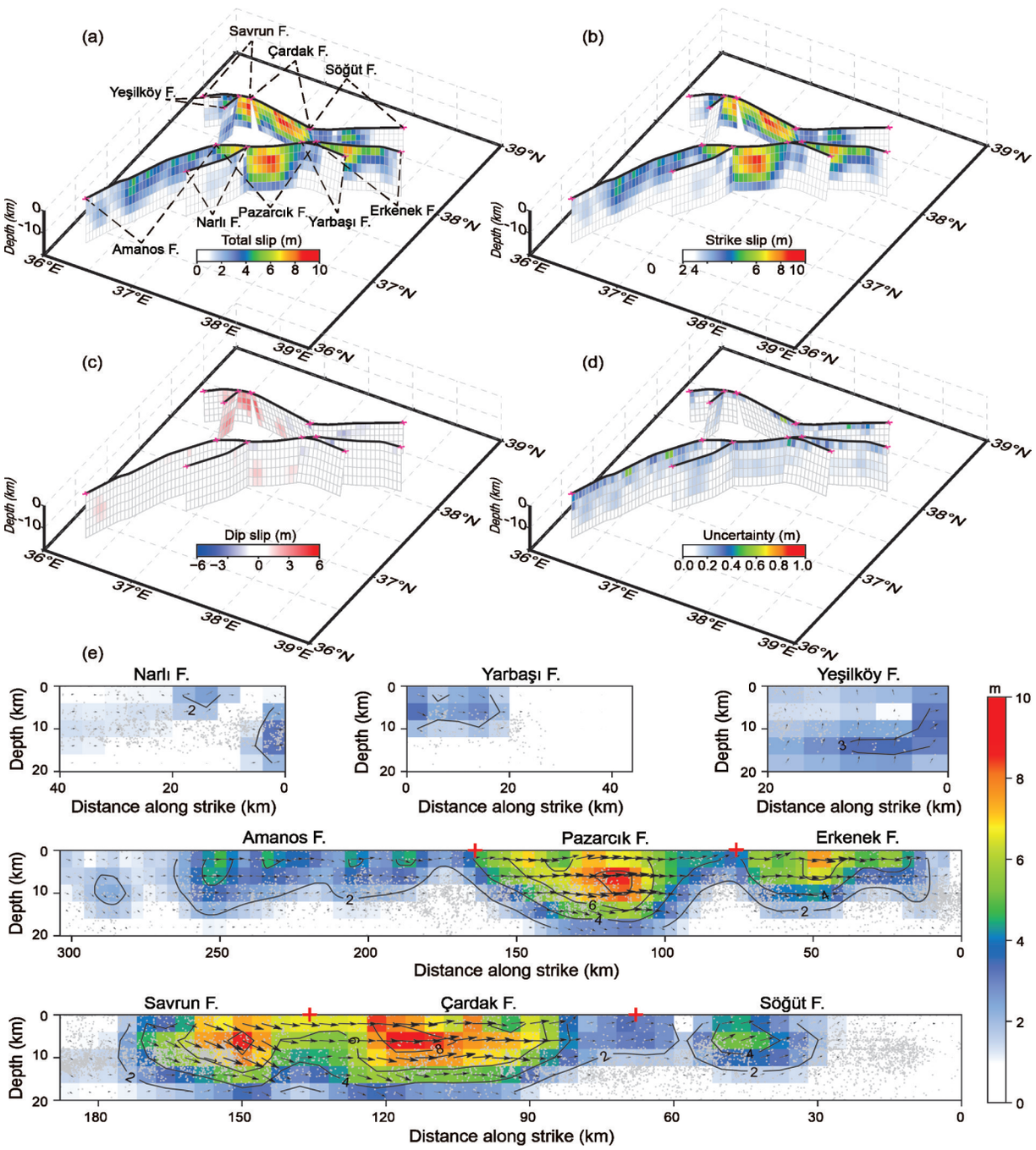


**Figure 3.** Coseismic slip models of the 2023 Kahramanmaraş earthquake sequence. (a) Total slip distribution. (b) Strike-slip distribution. (c) Dip-slip distribution. (d) Uncertainty of the coseismic slip model. (e) 2D coseismic slip distribution along with the distribution of precise aftershocks (gray dots), with black solid lines representing coseismic slip contours. Black arrows show movement of the hanging wall with respect to the footwall.

and 7.5 m, respectively. Additionally, several relatively small-sized asperities with peak slips around 5 m were found in the shallow section of the Amanos fault. For the $M_W$7.7 event, three major asperities were identified on the eastern segment of the Savrun fault, the mid-section of the Çardak fault, and the mid-section of the Söğüt fault, with peak slips of 8.7, 8.9, and 5.2 m, respectively. Unlike the other faults, the Yeşilköy fault is dominated by normal dip-slip, with a maximum slip of 3.3 m. Furthermore, a peak normal slip of up to 3.9 m was observed at a fault bend on the western side during the $M_W$7.7 event. According to He et al. (2023), this region, located at a releasing bend of the left-lateral strike-slip fault, is generally linked to extensional deformation and normal faulting structures (Cunningham and Mann, 2007). Ma et al. (2024) further pointed out that the Savrun fault and its branches create horsetail splay structures at the end of the strike-slip fault, which can naturally lead to normal-faulting earthquakes. Our fault slip distribution model is consistent with the studies of Barbot et al. (2023) and Jia et al. (2023), both of which accurately identified the main asperities in the ruptures of the Turkey earthquake doublet. They also observed significant SSD on the Pazarcık and Çardak faults. In contrast, the models of Zhang et al. (2023) and Ma et al. (2024) did not reveal notable SSD, which is likely due to the use of strong smoothing factor. In the following discussion section, we will further explore the reasons behind the significant differences in SSD estimates across existing studies. Assuming a shear modulus of 30 GPa, the moment released by the $M_W$7.8 and $M_W$7.7 events is approximately $5.00 \times 10^{20}$ N·m and $3.84 \times 10^{20}$ N·m , respectively, corresponding to $M_W$7.77 and $M_W$7.69.

The coseismic slip and aftershocks are generally distributed within a depth range of 0–16 km (Figure 3e), exhibiting a strong spatial complementarity. Aftershocks are primarily located around areas of high-slip and fault junctions, extending along both sides of the fault. The Jackknife resampling method was used to assess the reliability of the fault slip model (Zhao et al., 2023; Melgar et al., 2015). In this process, 75% of the dataset was randomly selected for each inversion, repeated 100 times, and the standard deviation for each subfault was calculated to determine model uncertainty (Figure 3d). Additionally, a checkerboard test was conducted on the coseismic slip distribution model using the same smoothing factor and weights to further confirm the model's reliability (Xu et al., 2023; Xu et al., 2017). The results of the checkerboard test (Figures S4a and S4b) indicate that the model successfully resolves fault slip, although the constraints from geodetic data diminish with increasing depth.

The predicted coseismic displacements of the Kahramanmaraş earthquake sequence from our preferred slip model fit well with the observations (Figures S5 and S6). The model misfits are 1.2 cm for the GPS data, 17.2 and 8.5 cm for the ALOS-2 ascending and descending track data, and 35.1 and 42.0 cm for the east-west and north-south deformation, respectively. Given that the accuracy of POT observations is much lower than that of GPS and DInSAR, it is anticipated that the RMS values for east-west and north-south deformations would be higher (Merryman Boncori, 2019).

## 3 DISCUSSION

### 3.1 Influence of Different Inversion Data on Slip Distribution

In this study, space geodetic data, including coseismic GPS displacements, LOS deformation from ALOS-2 ascending and descending tracks, and range and azimuth offsets from ALOS-2 and Sentinel-1 data, were used to constrain the fault geometry and slip distribution model. To assess how different datasets influence coseismic slip distribution, we compared the fault slip models inverted from using only GPS data, a combination of GPS and DInSAR data, and a combination of GPS, DInSAR, and POT data, referred to as model A, model B, and the preferred model, respectively. The comparison examines three main factors: (1) the impact on fault slip distribution; (2) the model's capacity to fit near-fault deformation; and (3) the resolution of the models.

The coseismic slip distribution models obtained using different datasets are shown in Figures 4a–4c. Model A exhibits a notably lower slip magnitude than the other two models. Unlike the $M_W$7.8 event, the fault slip for the $M_W$7.7 event in model A aligns more closely with the preferred model. This is likely due to the higher density of GPS stations surrounding the $M_W$7.7 event compared to the $M_W$7.8 event, especially the EKZ1 station located near the fault, which offers important constraints on the slip along the Çardak fault. Model B provides a more detailed slip distribution than model A and closely matches the preferred model. The primary differences between model B and the preferred model are observed in the shallow slip along the Pazarcık, Erkenek, Çardak, and Savrun faults, with model B predicting greater slip at depths of 0–4 km compared to the preferred model.

Figures 4d–4i show how different models fit the east-west and north-south displacements. Model A exhibits significant residuals in the areas close to the fault. In contrast, model B, which is based on DInSAR data, provides a much better fit for the observed deformation compared to model A, although it still does not match the near-fault deformation as effectively as the preferred model, especially along the Amanos fault south of the $M_W$7.8 event. The RMS values for model A, model B, and the preferred model are 87.1, 48.1, and 35.1 cm for the east-west direction, and 60.3, 49.7, and 42.0 cm for the north-south direction, respectively. Figure S4 presents the results of the checkerboard test for model A, model B, and the preferred model. As anticipated, Model A has the lowest resolution, making it challenging to accurately recover the synthetic slip distribution using only GPS data. The differences in the checkerboard test results between model B and the preferred model are mainly observed at depths of 0–4 km, where the preferred model shows higher resolution and a more precise recovery of the shallow fault slip.

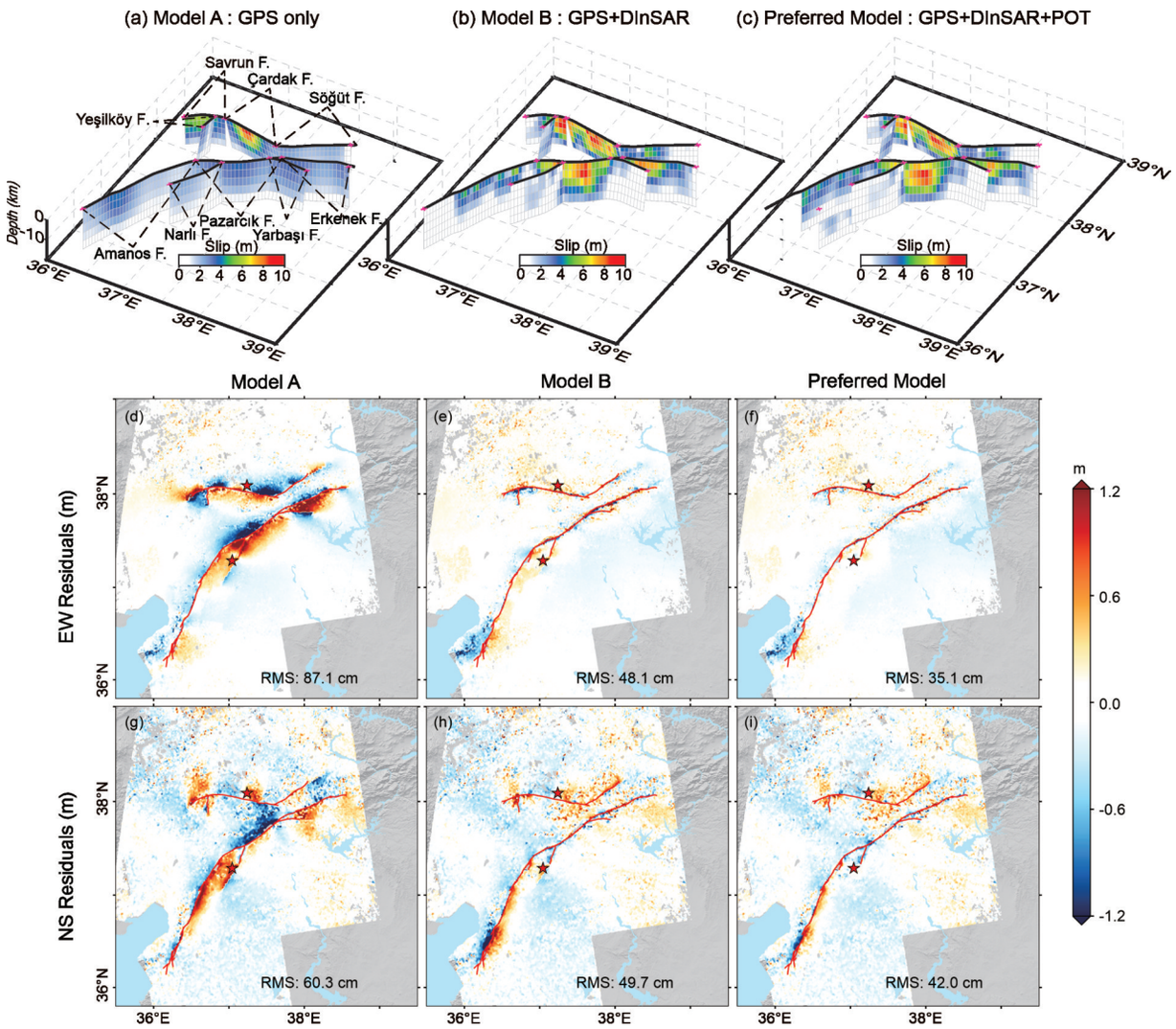


**Figure 4.** (a) Slip model estimated by GPS data. (b) Slip model estimated by GPS and DInSAR data. (c) Slip model estimated by GPS , DInSAR and POT data. (d)–(f) show the residuals in the east-west deformation for model A, model B, and the preferred model, respectively, while (g)–(l) present the residuals in the north-south deformation for model A, model B, and the preferred model, respectively.

The findings emphasize the value of utilizing multi-source data in joint inversion. The coseismic fault slip model derived from the integration of various data sources yields a more comprehensive slip distribution, aligns more closely with near-fault deformation, and demonstrates improved resolution. GPS data provides precise observations of coseismic deformation, thus it was given the most weight in the inversion process; however, its spatial resolution is the lowest one among the three datasets. DInSAR and POT data, known for their high spatial resolution, enhance the detail of the slip distribution and improve the model's resolution. Furthermore, the results highlight the importance of near-fault deformation. While POT data is not as accurate as GPS and DInSAR, it offers essential near-fault deformation information that better constrains shallow slip, thereby increasing the reliability of shallow fault slip estimates. The checkerboard test results for Model B also indicate that the $M_W$7.7 event's asperity in the shallow section of the Çardak fault is effectively captured, largely due to the significant constraints provided by the nearby EKZ1 station.

### 3.2 Factors Influencing the Estimation of Shallow Slip Deficit

Xu et al. (2016) suggested that SSD could be a result of insufficient near-fault data, and our finds in Section 3.1 also highlight the significance of near-fault deformation in accurately determining coseismic slip distribution. Besides near-fault data, the smoothing factor plays a role in estimating SSD. To assess how both the smoothing factor and near-fault data impact SSD estimation, we conducted two sets of simulation experiments. These simulations were based on the main fault from the Kahramanmaraş earthquake sequence, modelling the fault slip as purely left-lateral strike-slip. We utilized downsampled points from POT as near-field deformation data. Wang et al. (2024) noted that SSD is particularly sensitive to biased near-fault data, especially in the POT results. In our simulations, we obtained near-fault data directly from forward modelling of the synthetic model,

which allowed us to eliminate any bias in near-fault deformation.

We initially examined how the smoothing factor influences the estimation of SSD. To mitigate the impact of missing near-fault deformation, we included this data in our inversion dataset. We identified slip distribution models with under-smoothing, over-smoothing, and optimal smoothing (with corresponding smoothing factors of 0.003, 0.01, and 0.2, respectively) based on the trade-off curve between roughness and RMS (Jónsson et al., 2002). The choice of smoothing factor has a significant impact on the fault slip distribution and SSD estimation (Figure S7). As the smoothing factor increases, the peak slip in the model decreases, and the position of the maximum slip tends to move towards the top of the fault, a trend seen in numerous actual seismic events (Barbot et al., 2023; Jónsson et al., 2002). The SSD for the synthetic slip model was 20.0%, while the SSD values for smoothing factors of 0.003, 0.01, and 0.2 were 13.6%, 5.9%, and -7.8% (indicating no SSD), respectively. This indicates that applying smoothing constraints to the fault model can result in an underestimation of SSD.

We then assessed how near-field data affects the estimation of SSD. To reduce the impact of smoothing constraints, we chose a very small smoothing factor. We conducted inversions both with and without near-field deformation. The findings indicate that incorporating near-field deformation results in a more precise estimation of shallow fault slip (see Figure S8). The synthetic slip model shows an SSD of 20.0%, with an estimated SSD of 14.4% when near-field deformation is not considered, and 19.0% when it is included. Xu et al. (2016) noted that omitting near-field deformation often leads to an overestimation of SSD; however, our results, after reducing the influence of smoothing constraints, imply that lacking near-field data results in an underestimation of SSD. The discrepancy between these conclusions is likely due to the effects of smoothing constraints that significantly influence SSD estimation.

### 3.3 Shallow Slip Deficit of the 2023 Kahramanmaraş Earthquake Sequence

Significant strike-slip earthquakes, including the 1992 $M_W$7.3 Landers earthquake, the 1999 $M_W$7.1 Hector Mine earthquake, the 2010 $M_W$7.2 El Mayor-Cucapah earthquake, and the 2021 $M_W$7.4 Maduo earthquake, have shown evidence of SSD (e.g., Xu L et al., 2024; Xu W B et al., 2022; Jin and Fialko, 2021; Xu X H et al., 2016). A prevalent explanation for SSD, grounded in the rate-and-state friction law, posits that the velocity-strengthening region in the upper crust inhibits the spread of coseismic rupture, thus limiting shallow slip at the surface (e.g., Barbot et al., 2023; Xu et al., 2022; Jin and Fialko, 2021). This implies that some of the coseismic SSD may be offset by shallow interseismic creep or postseismic afterslip. For instance, the $M_W$6.8 Elazığ earthquake in 2020, which affected the central section of the EAFZ, exhibited a coseismic slip deficit of up to 60%. Further investigations indicated that the region with SSD also experienced interseismic creep and postseismic afterslip, where shallow creep impeded the seismic rupture's progression (Cakir et al., 2023; Pousse-Beltran et al., 2020). Another perspective on SSD suggests that inelastic deformation in the shallow crust could absorb some of the coseismic strain near the fault, which elastic slip models do not consider (Jin and Fialko, 2021; Fialko et al., 2005). Kaneko and Fialko (2011) noted that about 15% of SSD could be explained by including inelastic deformation in the model.

There is ongoing discussion in current research regarding the evaluation of SSD for the 2023 Kahramanmaraş Earthquake Sequence, with estimates varying from minimal to nearly 50% (e.g., Jiang et al., 2024; Barbot et al., 2023; Jia et al., 2023; Zhang et al., 2023). Zhang et al. (2023) did not identify SSD in their model based on Sentinel-1 and GPS data, which may be due to a strong smoothing factor and the exclusion of near-fault deformation, as significant decorrelation occurs in the Sentinel data close to the fault. To tackle the severe decorrelation issues linked to Sentinel data when measuring deformation from large earthquakes near the fault, Jiang et al. (2024) introduced an enhanced SNAPHU phase unwrapping algorithm (P-SNAPHU). Using the unwrapped results from P-SNAPHU, the SSD for the 2023 Kahramanmaraş earthquake sequence is estimated to be around 7%. Ma et al. (2024) limited the inversion of the slip model using extensive space geodetic data, yielding an SSD of less than 5%, likely due to the application of strong smoothing constraints. To achieve a more precise SSD estimate, Wang et al. (2024) excluded biased near-fault data, resulting in the SSD for the $M_W$7.8 and $M_W$7.7 events being reduced from 44% and 53% to 6% and 22%, respectively. In this study, we estimated the SSD as 16%, 5%, and 22% for the Pazarcık, Çardak, and Savrun faults, respectively.

Interseismic creep, afterslip, or diffuse deformation can compensate for SSD (Jia et al., 2023). Weiss et al. (2020) analyzed nearly five years of data from Sentinel-1 and GPS to assess surface velocity and tectonic strain accumulation throughout the Anatolian region. Their findings indicated that significant localized strain accumulation was present only in the northeastern section of the EAFZ, with no clear evidence of interseismic creep at the fault involved in the 2023 Kahramanmaraş earthquake sequence. Xu et al. (2023) utilized DInSAR techniques to observe postseismic deformation for two months after the Kahramanmaraş earthquake sequence. The ascending track data showed no notable differences in deformation gradients on either side of the Pazarcık and Çardak faults, while the descending track data experienced severe decorrelation near the fault. Further observations are needed to determine if afterslip played a role in compensating for SSD. Based on the ascending track data alone, the impact of afterslip on SSD seems minimal. Provost et al. (2024) employed high-resolution coseismic fault offsets from Sentinel-2 imagery to estimate the dif-

fuse deformation associated with the Kahramanmaraş earthquake sequence, finding that the $M_W$7.8 and $M_W$7.7 events had 54% and 47% diffuse deformation, respectively. Importantly, the diffuse deformation of the Çardak fault was under 30%, aligning with the relatively low SSD estimated for that fault. In conclusion, we believe that the SSD of the Kahramanmaraş earthquake sequence is mainly compensated by the diffuse deformation around the fault.

## 4 CONCLUSION

Space geodetic observations are vital for providing important data constraints for modelling earthquake source parameters and are key to investigating rupture characteristics. In this study, we utilized ALOS-2 and Sentinel-1 images to reconstruct a complete 3D deformation field for the Kahramanmaraş earthquake sequence. The preferred slip distribution model, estimated using GPS, InSAR, and POT data, indicates that the Kahramanmaraş earthquake sequence was primarily characterized by left-lateral strike-slip movement. The maximum slip for the $M_W$7.8 and $M_W$7.7 events were 8.5 and 8.9 m, respectively, both occurring at depths of 4–8 km. Additionally, we examined the ongoing debate in previous studies about the estimation of the SSD for the Kahramanmaraş earthquake sequence, concluding that the selection of smoothing factors and the inclusion of near-fault deformation data are critical factors contributing to the significant discrepancies in SSD estimates among various studies. The high smoothing factor, in particular, can lead to a significant underestimation of the SSD.

## ACKNOWLEDGMENTS

The Sentinel-1 SAR images are provided by the European Space Agency (https://dataspace. copernicus. eu/). The coseismic ALOS-2 SAR images are provided by the Japan Aerospace Exploration Agency and are publicly available for download at https://www. eorc. jaxa. jp/ALOS/jp/dataset/open_and_free/JAXA_ALOS-2_PALSAR-2_ScanSAR_turkey_L1.1_Link_20230228.html. The GPS data are downloaded from the Nevada Geodetic Laboratory (http://geodesy.unr.edu/). This work was supported by the National Natural Science Foundation of China (Nos. 42174023, 42304037), the National Key Research and Development Program (No. 2022YFB3903602), the Natural Science Foundation of Hunan Province (No. 2024JJ3031), the Frontier Cross Research Project of Central South University (No. 2023QYJC006). The figures in this work were generated by the Generic Mapping Tools (Wessel et al., 2013). The final publication is available at Springer via https://doi. org/10.1007/s12583-024-0146-5.

**Electronic Supplementary Materials:** Supplementary materials (Figures S1–S8; Table S1) are available in the online version of this article at https://doi. org/10.1007/s12583-024-0146-5.

## Conflict of Interest

The authors declare that they have no conflict of interest.

## REFERENCES CITED

Aktug, B., Ozener, H., Dogru, A., et al., 2016. Slip Rates and Seismic Potential on the East Anatolian Fault System Using an Improved GPS Velocity Field. *Journal of Geodynamics*, 94: 1–12. https://doi.org/10.1016/j.jog.2016.01.001

Barbot, S., Luo, H., Wang, T., et al., 2023. Slip Distribution of the February 6, 2023 $M_W$7.8 and $M_W$7.6, Kahramanmaraş, Turkey Earthquake Sequence in the East Anatolian Fault Zone. *Seismica*, 2(3): 1–17. https://doi.org/10.26443/seismica.v2i3.502

Bayrak, E., Yılmaz, Ş., Softa, M., et al., 2015. Earthquake Hazard Analysis for East Anatolian Fault Zone, Turkey. *Natural Hazards*, 76(2): 1063–1077. https://doi.org/10.1007/s11069-014-1541-5

Bletery, Q., Cavalié, O., Nocquet, J. M., et al., 2020. Distribution of Interseismic Coupling along the North and East Anatolian Faults Inferred from InSAR and GPS Data. *Geophysical Research Letters*, 47(16): e2020GL087775. https://doi. org/10.1029/2020gl087775

Blewitt, G., Hammond, W., Kreemer, C., 2018. Harnessing the GPS Data Explosion for Interdisciplinary Science. *Eos*, 99, https://doi.org/10.1029/2018eo104623

Cakir, Z., Doğan, U., Akoğlu, A. M., et al., 2023. Arrest of the $M_W$6.8 January 24, 2020 Elaziğ (Turkey) Earthquake by Shallow Fault Creep. *Earth and Planetary Science Letters*, 608: 118085. https://doi.org/10.1016/j.epsl.2023.118085

Chen, C. W., Zebker, H. A., 2002. Phase Unwrapping for Large SAR Interferograms: Statistical Segmentation and Generalized Network Models. *IEEE Transactions on Geoscience and Remote Sensing*, 40(8): 1709–1719. https://doi.org/10.1109/tgrs.2002.802453

Chen, W. K., Rao, G., Kang, D. J., et al., 2023. Early Report of the Source Characteristics, Ground Motions, and Casualty Estimates of the 2023 $M_W$7.8 and 7.5 Turkey Earthquakes. *Journal of Earth Science*, 34(2): 297–303. https://doi. org/10.1007/s12583-023-1316-6

Cunningham, W. D., Mann, P., 2007. Tectonics of Strike-Slip Restraining and Releasing Bends. *Geological Society of London Special Publications*, 290(1): 1–12. https://doi. org/10.1144/sp290.1

Duman, T. Y., Emre, Ö., 2013. The East Anatolian Fault: Geometry, Segmentation and Jog Characteristics. *Geological Society, London, Special Publications*, 372(1): 495–529. https://doi. org/10.1144/sp372.14

Fang, N., Sun, K., Huang, C., et al., 2024. Joint Inversion of InSAR and Seismic Data for the Kinematic Rupture Process of the 2023 $M_S$6.2 Jishishan Earthquake. Geomatics and Information Science of Wuhan University. https://doi.org/10.13203/j.whugis20240036 (in Chinese with English Abstract)

Fialko, Y., Sandwell, D., Simons, M., et al., 2005. Three-Dimensional Deformation Caused by the Bam, Iran, Earthquake and the Origin of Shallow Slip Deficit. *Nature*, 435(7040): 295–299. https://doi.org/10.1038/nature03425

Gao, H., Liao, M., Feng, G., 2021. An Improved Quadtree Sampling Method for InSAR Seismic Deformation Inversion. *Remote Sensing*, 13(9): 1678. https://www. mdpi. com/2072-4292/13/9/

1678

Goldstein, R. M., Werner, C. L., 1998. Radar Interferogram Filtering for Geophysical Applications. *Geophysical Research Letters*, 25(21): 4035–4038. https://doi.org/10.1029/1998gl900033

He, K. F., Wen, Y. M., Xu, C. J., et al., 2022. Fault Geometry and Slip Distribution of the 2021 $M_W$7.4 Maduo, China, Earthquake Inferred from InSAR Measurements and Relocated Aftershocks. *Seismological Research Letters*, 93(1): 8–20. https://doi.org/10.1785/0220210204

He, L. J., Feng, G. C., Xu, W. B., et al., 2023. Coseismic Kinematics of the 2023 Kahramanmaras, Turkey Earthquake Sequence from InSAR and Optical Data. *Geophysical Research Letters*, 50(17): e2023GL104693. https://doi.org/10.1029/2023gl104693

He, P., Wen, Y. M., Wang, X. H., et al., 2024. The N-S Direction Strike-Slip Activities in the Pamir Hinterland under Oblique Convergence: The 2015 and 2023 Earthquakes. *Geophysical Journal International*, 238(2): 1150–1163. https://doi.org/10.1093/gji/ggae214

Hu, J., Li, Z. W., Ding, X. L., et al., 2014. Resolving Three-Dimensional Surface Displacements from InSAR Measurements: A Review. *Earth-Science Reviews*, 133: 1–17. https://doi.org/10.1016/j.earscirev.2014.02.005

Jia, Z., Jin, Z. Y., Marchandon, M., et al., 2023. The Complex Dynamics of the 2023 Kahramanmaraş, Turkey, $M_W$7.8 – 7.7 Earthquake Doublet. *Science*, 381(6661): 985–990. https://doi.org/10.1126/science.adi0685

Jiang, K., Xu, W. B., Xie, L., 2024. Unwrap Intractable C-Band Coseismic Interferograms: An Improved SNAPHU Method with Range Offset Gradients as Prior Information. *Journal of Geophysical Research*: *Solid Earth*, 129(10): e2024JB028826. https://doi.org/10.1029/2024jb028826

Jin, Z. Y., Fialko, Y., 2021. Coseismic and Early Postseismic Deformation due to the 2021 *M*7.4 Maduo (China) Earthquake. *Geophysical Research Letters*, 48(21): e2021GL095213. https://doi.org/10.1029/2021gl095213

Jónsson, S., 2002. Fault Slip Distribution of the 1999 $M_W$7.1 Hector Mine, California, Earthquake, Estimated from Satellite Radar and GPS Measurements. *Bulletin of the Seismological Society of America*, 92(4): 1377–1389. https://doi.org/10.1785/0120000922

Kaneko, Y., Fialko, Y., 2011. Shallow Slip Deficit Due to Large Strike-Slip Earthquakes in Dynamic Rupture Simulations with Elasto-Plastic Off-Fault Response. *Geophysical Journal International*, 186(3): 1389–1403. https://doi.org/10.1111/j.1365-246x.2011.05117.x

Kusky, T. M., Bozkurt, E., Meng, J. N., et al., 2023. Twin Earthquakes Devastate Southeast Türkiye and Syria: First Report from the Epicenters. *Journal of Earth Science*, 34(2): 291–296. https://doi.org/10.1007/s12583-023-1317-5

Li, Z. W., Xu, W. B., Hu, J., et al., 2022. Partial Geoscience Parameters Inversion from InSAR Observation. *Acta Geodaetica et Cartographica Sinica*, 51(7): 1458 – 1475 (in Chinese with English Abstract)

Lomax, A., 2023. Precise, NLL-SSST-Coherence Hypocenter Catalog for the 2023 $M_W$7.8 and $M_W$7.6 SE Turkey Earthquake Sequence. v3.0 [Data Set], Zenodo, https://doi. org/10.5281/zenodo.8089273

Ma, Z. F., Li, C. L., Jiang, Y., et al., 2024. Space Geodetic Insights to the Dramatic Stress Rotation Induced by the February 2023 Turkey-Syria Earthquake Doublet. *Geophysical Research Letters*, 51(6): e2023GL107788. https://doi. org/10.1029/2023gl107788

Melgar, D., Geng, J. H., Crowell, B. W., et al., 2015. Seismogeodesy of the 2014 $M_W$6.1 Napa Earthquake, California: Rapid Response and Modeling of Fast Rupture on a Dipping Strike-Slip Fault. *Journal of Geophysical Research*: *Solid Earth*, 120(7): 5013–5033. https://doi.org/10.1002/2015jb011921

Merryman Boncori, J. P., 2019. Measuring Coseismic Deformation with Spaceborne Synthetic Aperture Radar: A Review. *Frontiers in Earth Science*, 7: 16. https://doi.org/10.3389/feart.2019.00016

Nalbant, S. S., McCloskey, J., Steacy, S., et al., 2002. Stress Accumulation and Increased Seismic Risk in Eastern Turkey. *Earth and Planetary Science Letters*, 195(3/4): 291–298. https://doi.org/10.1016/s0012-821x(01)00592-1

Okada, Y., 1985. Surface Deformation Due to Shear and Tensile Faults in a Half-Space. *Bulletin of the Seismological Society of America*, 75(4): 1135–1154. https://doi.org/10.1785/bssa0750041135

Pousse-Beltran, L., Nissen, E., Bergman, E. A., et al., 2020. The 2020 $M_W$6.8 Elazığ (Turkey) Earthquake Reveals Rupture Behavior of the East Anatolian Fault. *Geophysical Research Letters*, 47(13): e2020GL088136. https://doi.org/10.1029/2020gl088136

Provost, F., Karabacak, V., Malet, J. P., et al., 2024. High-Resolution Co-Seismic Fault Offsets of the 2023 Türkiye Earthquake Ruptures Using Satellite Imagery. *Scientific Reports*, 14(1): 6834. https://doi.org/10.1038/s41598-024-55009-5

Reilinger, R., McClusky, S., Vernant, P., et al., 2006. GPS Constraints on Continental Deformation in the Africa-Arabia-Eurasia Continental Collision Zone and Implications for the Dynamics of Plate Interactions. *Journal of Geophysical Research*: *Solid Earth*, 111(B5): B05411. https://doi.org/10.1029/2005jb004051

Reitman, N. G., Briggs, R. W., Barnhart, W. D., et al., 2023. Fault Rupture Mapping of the 6 February 2023 Kahramanmaraş, Türkiye, Earthquake Sequence from Satellite Data. U. S. Geological Survey Data Release, ver. 1.1

Simão, N. M., Nalbant, S. S., Sunbul, F., et al., 2016. Central and Eastern Anatolian Crustal Deformation Rate and Velocity Fields Derived from GPS and Earthquake Data. *Earth and Planetary Science Letters*, 433: 89–98. https://doi.org/10.1016/j.epsl.2015.10.041

Wang, K., Fialko, Y., 2014. Space Geodetic Observations and Models of Postseismic Deformation due to the 2005 *M*7.6 Kashmir (Pakistan) Earthquake. *Journal of Geophysical Research*: *Solid Earth*, 119(9): 7306–7318. https://doi.org/10.1002/2014jb011122

Wang, K., Xu, X. H., Hu, Y., 2024. Kinematics of the 2023 Kahramanmaraş Earthquake Doublet: Biased Near-Fault Data and Shallow Slip Deficit. *Seismological Research Letters*, https://doi.org/10.1785/0220240062

Wang, R., Parolai, S., Ge, M., et al., 2013. The 2011 $M_W$9.0 Tohoku Earthquake: Comparison of GPS and Strong-Motion Data. *Bulletin of the Seismological Society of America*, 103(2B): 1336–1347. https://doi.org/10.1785/0120110264

Weiss, J. R., Walters, R. J., Morishita, Y., et al., 2020. High-

Resolution Surface Velocities and Strain for Anatolia from Sentinel-1 InSAR and GNSS Data. *Geophysical Research Letters*, 47(17): e2020GL087376. https://doi.org/10.1029/2020gl087376

Werner, C., Wegmüller, U., Strozzi, T., et al., 2000. Gamma Sar and Interferometric Processing Software. *Proceedings of the Ers-Envisat Symposium*, *Gothenburg*, *Sweden*, 1620: 1620

Wessel, P., Smith, W. H. F., Scharroo, R., et al., 2013. Generic Mapping Tools: Improved Version Released. *Eos*, *Transactions American Geophysical Union*, 94(45): 409–410. https://doi.org/10.1002/2013eo450001

Xu, C. J., Zhou, L. X., Yin, Z., 2017. Construction and Geodesy Slip Inversion Analysis of 2013 $M_S$7.0 Lushan in China Earthquake's Curved Fault Model. *Geomatics and Information Science of Wuhan University*, 42(11): 1665–1672 (in Chinese with English Abstract)

Xu, L., Aoki, Y., Wang, J. Q., et al., 2024. The 2023 $M_W$7.8 and 7.6 Earthquake Doublet in Southeast Türkiye: Coseismic and Early Postseismic Deformation, Faulting Model, and Potential Seismic Hazard. *Seismological Research Letters*, 95(2A): 562 – 573. https://doi.org/10.1785/0220230146

Xu, W. B., Feng, G. C., Meng, L. S., et al., 2018. Transpressional Rupture Cascade of the 2016 $M_W$7.8 Kaikoura Earthquake, New Zealand. *Journal of Geophysical Research*: *Solid Earth*, 123(3): 2396–2409. https://doi.org/10.1002/2017jb015168

Xu, W. B., Liu, X. G., Bürgmann, R., et al., 2022. Space Geodetic Evidence of Basement-Involved Thick-Skinned Orogeny and Fault Frictional Heterogeneity of the Papuan Fold Belt, Papua New Guinea. *Journal of Geophysical Research*: *Solid Earth*, 127(8): e2022JB024227. https://doi.org/10.1029/2022jb024227

Xu, X. H., Tong, X. P., Sandwell, D. T., et al., 2016. Refining the Shallow Slip Deficit. *Geophysical Journal International*, 204(3): 1867–1886. https://doi.org/10.1093/gji/ggv563

Zhang, Y. J., Tang, X. W., Liu, D. C., et al., 2023. Geometric Controls on Cascading Rupture of the 2023 Kahramanmaraş Earthquake Doublet. *Nature Geoscience*, 16: 1054 – 1060. https://doi.org/10.1038/s41561-023-01283-3

Zhao, L., Xu, W., Xie, L., et al., 2023. Fault Geometry and Low Frictional Control of the Near-Field Postseismic Deformation of the 2021 $M_W$7.3 Maduo Earthquake. *Tectonophysics*, 863: 230000 (in Chinese with English Abstract)